Eye-Readable Detection and Oxidation of CO with a Platinum-Based Catalyst and a Binuclear Rhodium Complex

Jiafu Qu, Yueqiang Cao, Xuezhi Duan, Najun Li, Qingfeng Xu, Hua Li, Jinghui He, Dongyun Chen,* and Jianmei Lu*

Abstract: Toxic gases that are colorless and odorless, such as CO, are a major environmental concern and require early detection to prevent serious toxicological effects. In this study, a unique system (Pt/HMSs-BRC) was fabricated by combining a catalyst (Pt/hollow mesoporous silica spheres, Pt/HMSs) with a silica gel containing an adsorbed chromogenic probe (binuclear rhodium complex, BRC). The process is a simple method to prepare well-dispersed and uniform Pt nanoparticles. The Pt/HMSs-BRC materials demonstrated early CO detection and excellent catalytic performance for CO oxidation. The probe exhibited remarkable color modulation from gray-violet to light-yellow when exposed to CO concentration levels above 50 ppm, and the color of the chromogenic probe was fully recoverable. By a kinetics-assisted discrimination method and DFT calculations, it was found that the corner Pt sites are the dominant active sites for CO oxidation.

Introduction

It has been increasingly recognized that air pollution has wide-ranging and deleterious effects on human health, and is a major global concern.[1] CO is a common air pollutant emitted in exhaust gases.[2] CO is highly toxic, as it can quickly combine with hemoglobin, and is particularly difficult to detect, as it is colorless and odorless.[3] The threshold level at which CO is considered toxic is at concentrations exceeding 50 ppm, which can quickly result in dizziness, unconsciousness, and even death.[4] As the symptoms are often overlooked, fatalities result if exposure is not detected. There are many unintentional deaths in China alone each year attributed to CO poisoning.[5] Therefore, considerable efforts have been made to detect and treat CO pollution to improve air quality. The majority of existing CO sensors utilize electro-chemical-cell, solid-state-sensor, and thermocouple technologies.[6] However, it remains a challenge to perform accurate measurements on real samples as a result of the sensors being able to only detect CO in solution and not air, thus requiring relatively large detection limits, and displaying poor color modulation.[4] Therefore, there is strong interest in developing an eye-readable CO sensor that can readily detect the presence of CO above the concentration threshold at which CO is toxic. Herein, a binuclear rhodium complex (BRC) is proposed as a CO sensor because of unambiguous color modulation as well as CO sensitivity and selectivity in the gas phase.

An attractive approach for the treatment of CO pollution is by catalytic oxidation to CO_2.[7] Among the tested catalysts, noble metals (especially platinum) are extremely efficient heterogeneous catalysts.[8] Although platinum plays a pivotal role in heterogeneous catalysis, it is rare and is without adequate alternatives.[9] To address the problem, a variety of supported Pt catalysts have been used for the catalytic conversion of CO into CO_2.[10] In particular, platinum-supported oxide systems exhibit enhanced catalytic performance as a result of a possible synergistic effect. Previous reports have demonstrated the use of various oxides as the catalyst support, such as CeO_2, SiO_2, TiO_2, Fe_2O_3, and ZrO_2.[11] The advantages of using silica-based materials as support materials are their low cost, well-defined nanostructure, high surface area, and excellent thermal stability.[12] Kröcher and co-workers reported a simple method for obtaining Pt/SiO_2 catalysts, which exhibited good catalytic activity for NO oxidation.[13] Alternatively, Lu and co-workers synthesized $Pt@SiO_2$ core–shell nanocomposites for the catalytic generation of hydrogen.[14] Although widely used in heterogeneous catalysis, the synthesis of well-dispersed Pt nanoparticles (NPs) possessing a narrow particle size distribution of an appropriate tailored size within the channels of silica remains a challenge.

There are numerous reports on the catalytic oxidation of CO and the detection of CO by semiconducting metal oxides.[15] However, the simultaneous detection and catalytic oxidation of CO by a combined catalytic approach that comprises both a CO-sensing probe and a catalyst is rare. In this study, hollow mesoporous silica spheres (HMSs) that support the Pt NP catalysts were synthesized by a selective etching strategy.[16] The highly monodisperse Pt NPs mostly reside at the pores of the HMS support and possess a uniform size and shape. Thereafter, the chromogenic probe is adsorbed onto silica gel and combined with the Pt/HMSs catalyst to allow for the simultaneous detection and catalytic

[*] Dr. J. Qu, Prof. N. Li, Prof. Q. Xu, Prof. H. Li, Prof. J. He, Prof. D. Chen, Prof. J. Lu
College of Chemistry, Chemical Engineering and Materials Science
Collaborative Innovation Center of Suzhou Nano Science and Technology, Soochow University
Suzhou 215123 (P. R. China)
E-mail: dychen@suda.edu.cn
            lujm@suda.edu.cn

Dr. Y. Cao, Prof. X. Duan
State Key Laboratory of Chemical Engineering
East China University of Science and Technology
Shanghai 200237 (China)

Supporting information and the ORCID identification number(s) for the author(s) of this article can be found under:
https://doi.org/10.1002/anie.201905567.

■■■■ Wiley Online Library

© 2019 Wiley-VCH Verlag GmbH & Co. KGaA, Weinheim

Angew. Chem. Int. Ed. **2019**, *58*, 2–8

↖↗ These are not the final page numbers!

conversion of CO (see Scheme 1). Silica gel was chosen as the material to integrate the catalyst and probe owing to its good adsorption and thermal stability. Pt/HMSs were able to convert 100% of the CO, while the chromogenic probe
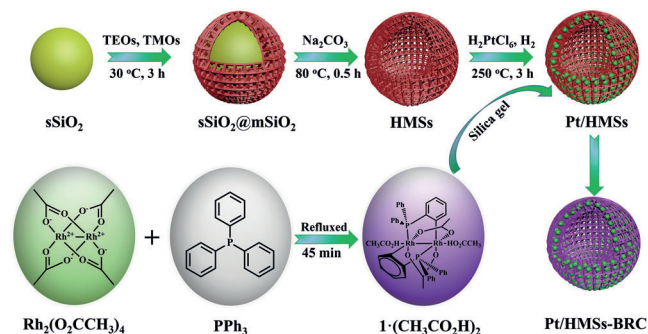
Scheme 1. Fabrication of a combined catalyst (Pt/HMSs-BRC).

displayed remarkable color modulation at CO concentration levels above 50 ppm. Interestingly, the color modulation in this system is fully recoverable. Furthermore, the active sites of CO oxidation over Pt/HMSs was investigated using a kinetics-assisted discrimination method and DFT calculations. Our results demonstrate that the corner sites of Pt are the dominant active sites for CO oxidation, which could aid the design of highly active catalysts for CO oxidation. Therefore, this combined catalyst approach, or a similar system, has the potential to be applied to the detection and removal of the colorless and odorless hazard CO.

Results and Discussion

Monodisperse sSiO$_2$@mSiO$_2$ core–shell NPs were synthesized by a facile method.[16] Transmission electron microscopy (TEM) and scanning electron microscopy (SEM) images of the homogeneous core–shell structures are shown in Figure 1a,b. The core–shell structures are monodisperse and exhibit a narrow particle size distribution of approximately 412 nm (Figure 1c). As can be observed from the micrographs, the particles exhibit near-perfect spherical morphology with no apparent aggregation. Subsequently, HMSs were obtained by selective etching with a Na$_2$CO$_3$ solution prior to calcination. The samples were then subjected to calcination in air at 550°C for 6 h to remove the surfactants. The HMSs are highly disperse, and no significant structural changes to the HMSs were observed after calcination (Figure 1d,e,g,h). As shown in Figure 1d,g, a uniform hollow pore (approximately 294 nm, Figure 1f) and a mesoporous SiO$_2$ shell (approximately 53 nm, Figure 1i) were obtained. The SEM images in Figure 1e,h also demonstrate the synthesis of complete and uniform HMSs.

Pt NPs were encapsulated in the HMS pore structure by a vacuum-assisted incipient wetness impregnation method. The pores of the HMSs act as containers to control the Pt NP growth. Interestingly, the major population of Pt NPs reside in the HMS pores rather than on the external surface of the support when this method is used. SEM images of Pt/HMSs
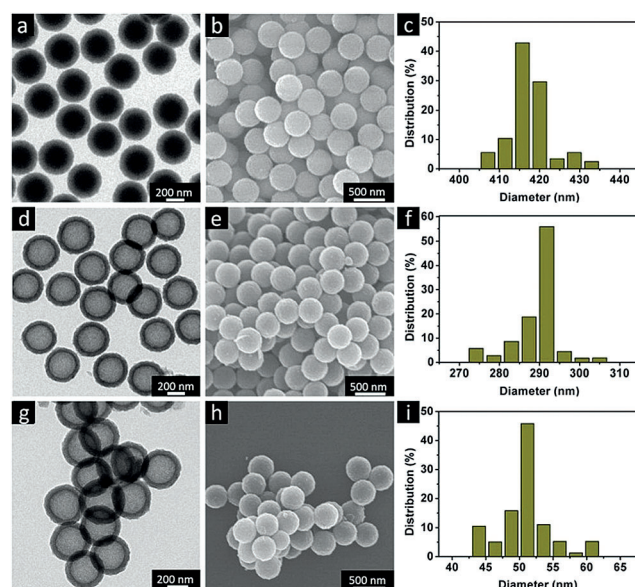
Figure 1. a) TEM and b) SEM images of sSiO$_2$@mSiO$_2$; d) TEM and e) SEM micrographs of HMSs before calcination; g) TEM and h) SEM micrographs of HMSs after calcination; c) total, f) inner, and i) outer diameter distribution histograms of HMSs from SEM and TEM image analysis.

(Figure 2a; see also Figure S1b in the Supporting Information). There are no observable differences to the HMSs prior to Pt loading (Figure 1h; see also Figure S1a), thus indicating that the majority of Pt NPs are loaded in the HMS pores rather than residing at the external surface. Low-magnification and high-magnification TEM images of Pt/HMSs (Figure 2b,c) show that the Pt NPs were successfully loaded in/on
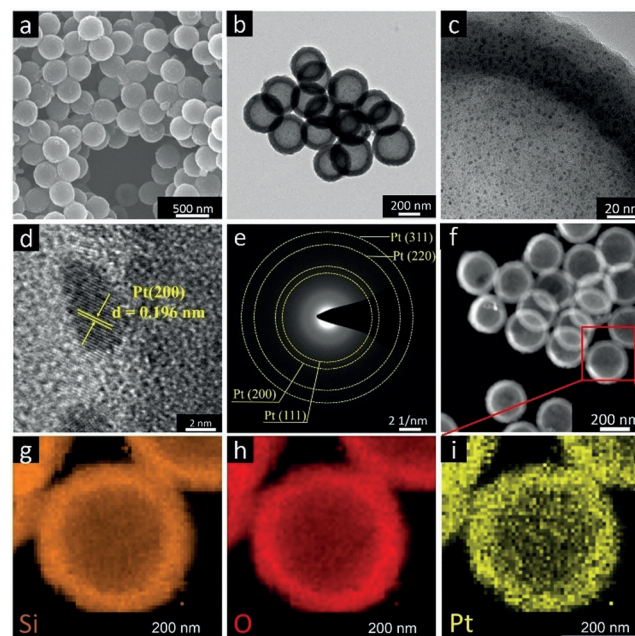
Figure 2. a) SEM, b,c) TEM, d) HRTEM, and e) SAED micrographs of 5.0 wt% Pt/HMSs; f) HAADF-STEM image of 5.0 wt% Pt/HMSs; g–i) STEM EDX mapping of Si (g), O (h), and Pt (i).

the HMSs, and had a homogeneous and narrow size distribution centered at approximately 3 nm (see Figure S2).

Scanning transmission electron microscopy (STEM) of multiple Pt/HMSs samples (see Figure S2) further confirmed that Pt NPs were homogeneously dispersed on HMSs. We performed inductively coupled plasma (ICP) analysis to determine Pt loading levels in HMSs (see Table S1 in the Supporting Information). The actual content of Pt NPs in the different catalysts were 0.41, 1.30, and 2.32 wt%. Brunauer–Emmett–Teller (BET) surface area measurements were performed on HMSs and Pt/HMSs samples, and their pore sizes calculated using the Barrett–Joyner–Halenda (BJH) model (see Figure S3 and Table S1). The catalysts exhibited type IV isotherms as indicated by the narrow hysteresis loops, thus indicating that the HMSs catalysts possess mesoporous structures. The corresponding pore size distribution indicates that the catalyst pore size is principally distributed between 3.0 and 4.0 nm (see Figure S3).

The presence of Pt NPs was also confirmed by high-resolution TEM (HRTEM; Figure 2 d). An interplanar lattice spacing of 0.196 nm was observed, which is consistent with the (200) crystallographic plane of Pt. The bright diffraction rings in the selected area electron diffraction (SAED) pattern (Figure 2 e) further confirm the presence of Pt NPs. A typical high-angle annular dark-field scanning transmission electron microscopy (HAADF-STEM) image (Figure 2 f) showed that Pt NPs are distributed in discrete disordered locations. Furthermore, the chemical composition of the catalyst was further confirmed by STEM energy dispersive X-ray (EDX) mapping (Figure 2 i), which revealed the uniform presence of Pt on the HMSs.

Powder X-ray diffraction (XRD) was used to analyze the crystallinity and phase structure of Pt/HMSs (see Figure S4), and the chemical state and surface composition of the catalysts were further investigated by X-ray photoelectron spectroscopy (XPS; Figure 3). The expected Si, O, and Pt peaks were observed in the XPS survey spectrum (Figure 3 a), which indicates the successful synthesis of the catalyst. For the

HMSs sample, the Si 2p spectrum (Figure 3 b) was symmetrical with a corresponding binding energy of 103.5 eV, in complete accordance with the reported value.[17] Figure 3 c shows the Pt 4f deconvolution spectra as a function of platinum loading. The Pt NP binding energies are derived from the Pt $4f_{5/2}$ and Pt $4f_{7/2}$ spectra (see Table S1). The Pt $4f_{7/2}$ spectra were fitted using three different states corresponding to binding energies of approximately 71.0, 72.5, and 73.8 eV, attributed to Pt^0, Pt^{2+}, and Pt^{4+}, respectively. The Pt 4f chemical shifts of Pt^{2+} and Pt^{4+} relative to Pt^0 are approximately 1.5 and 2.8 eV, respectively.

Previous studies demonstrated that a BRC compound was not only highly selective, but could also undergo a complete and reversible reaction with CO.[4] Therefore, this BRC was chosen as the probe for the detection of CO in air. The BRC compound (see Figure S5 for the structure) was synthesized by a previously reported procedure.[18] The structure of the product is composed of a binuclear dirhodium core bridged by *cis* acetate groups and two *ortho*-metal triphenylphosphine groups, with two acetic acid groups located at the axial sites (see Figure S6 for the NMR spectrum). When exposed to an air atmosphere containing carbon monoxide, the acetic acid groups occupying the axial sites are replaced with CO, and a concomitant color modulation from violet to orange-yellow is observed (see Figure S7 for the mechanism).

The catalytic activity of Pt/HMSs was investigated under an air atmosphere containing 1% CO as a function of Pt loading (Figure 4 a). The pure HMSs nanocatalyst, in the absence of Pt, displayed no catalytic activity, as observed by the lack of CO conversion. However, complete oxidation of CO to CO_2 occurred at temperatures of 205, 165, and 150°C for 1, 3, and 5 wt% Pt loading, respectively. Thus, increasing Pt loading resulted in a significant decrease in the temperature required for complete CO conversion. The 5 wt% Pt/
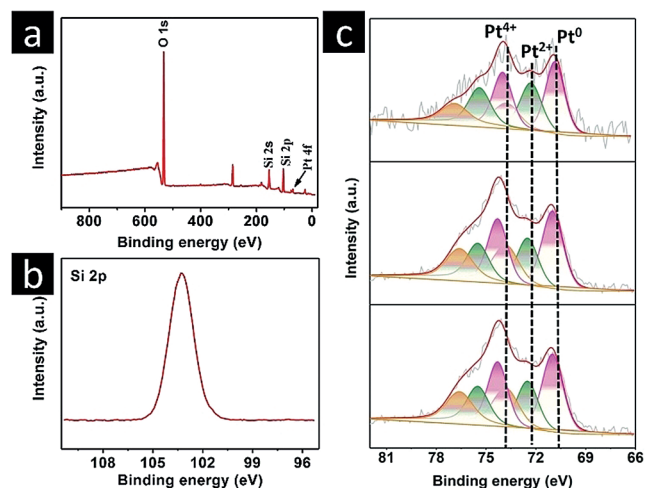

Figure 3. a) XPS survey spectrum of 5.0 wt% Pt/HMSs; b) high-resolution XPS spectrum of the Si 2p region of 5.0 wt% Pt/HMSs; c) deconvoluted Pt 4f spectra of 1.0 wt% (top), 3.0 wt% (middle), and 5.0 wt% Pt/HMSs (bottom).
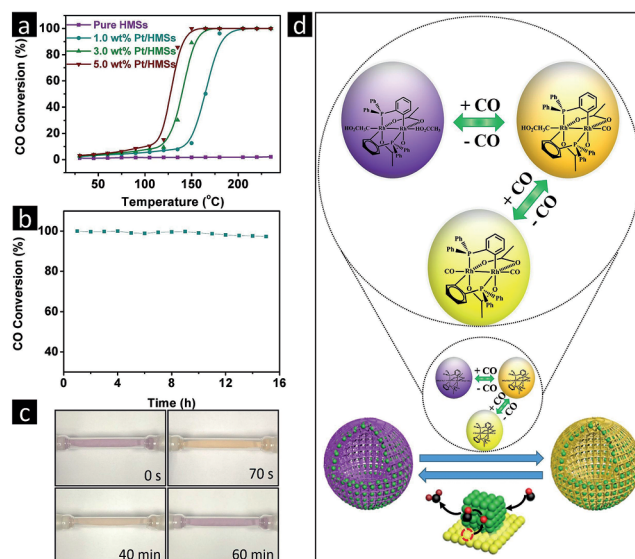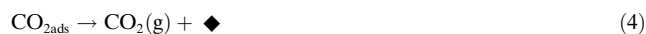

Figure 4. a) CO conversion as a function of reaction temperature; b) CO oxidation stability of 5.0 wt% Pt/HMSs at 150°C; c) photographs showing the color modulation of Pt/HMSs-BRC in contact with an air atmosphere containing CO (50 ppm); d) reaction mechanism for CO detection and removal.

HMSs catalyst showed better performance for CO oxidation than previously reported catalysts (see Table S2), and its CO oxidation activity (ca. 100% CO conversion) remained almost unchanged even after 15 h at 150°C (Figure 4b). A TEM image recorded after the reaction (see Figure S8) showed no aggregation of Pt NPs, thus further confirming the stability of the catalyst.

The colored Pt/HMSs-BRC system was exposed to air containing different concentrations of CO (see Table S3). Upon exposure to CO at a concentration of 50 ppm, a remarkable color change from gray-violet to light-yellow was observed after 70 s (Figure 4c). The Pt/HMSs catalysts were then used to catalyze the CO oxidation reaction. A hot air gun was used to heat, and activate, the catalysts to initiate CO oxidation. The color of the chromogenic probe was also observed to slowly recover with time, and the color of the system was fully recovered after 60 min. The reaction mechanism for the catalytic process is shown in Figure 4d.

The combination of the catalyst with the silica gel containing the adsorbed chromogenic probe resulted in a modified gray-violet solid. A remarkable color change from gray-violet to light-yellow was observed as a result of CO coordination at the axial positions. Thereafter, CO undergoes catalytic oxidation in the presence of Pt/HMSs, and the accepted reaction mechanism of CO oxidation on Pt can be explained by the Langmuir–Hinshelwood model.[11a] This process is shown in Equations (1)–(4). The color of the system is totally recoverable after the total oxidation of CO. Hence, a cycle involving the simultaneous detection and catalytic oxidation of CO is observed, where "◆" denotes a free adsorption site.

$$CO(g) + \blacklozenge \rightarrow CO_{ads} \tag{1}$$

$$O_2(g) + \blacklozenge \rightarrow 2\,O_{ads} \tag{2}$$

$$CO_{ads} + O_{ads} \rightarrow CO_{2ads} + \blacklozenge \tag{3}$$

$$CO_{2ads} \rightarrow CO_2(g) + \blacklozenge \tag{4}$$

The results of XPS suggest a similar electronic structure for differently sized Pt/HMSs catalysts, and thus the difference in the activity of these catalysts could be ascribed to the geometric structure, which can be demonstrated by understanding of the active sites. Kinetics-assisted discrimination was carried out to gain insight into the active sites of Pt/HMSs catalysts for CO oxidation. Figure 5a shows the reaction rate of differently sized Pt/HMSs catalysts, which varies with the particle size (d) as $d^{-3.6}$. If the surface sites, including the edge, corner, and terrace sites, exhibit the same activity for the reaction, the reaction rate normalized on the number of surface sites (i.e. TOF) should be independent of the particle size, and the reaction rate per total mole Pt atoms should vary with the particle size as d^{-1}. Thus, the sites exposed on the Pt surface exhibit different activity, probably owing to the different coordination environment.[19] The Arrhenius plots shown in Figure 5b provide the activation energy for these three catalysts. The activation energy found for CO oxidation over the differently sized Pt/HMSs catalysts was 72–75 kJ mol^{-1}, thus suggesting that the activation energy is
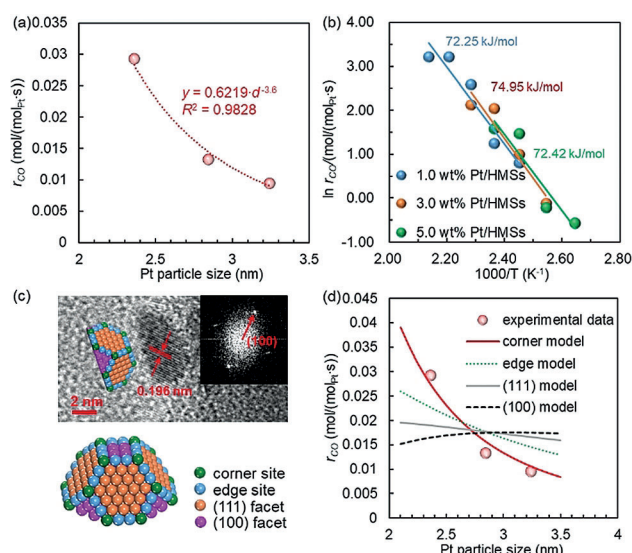

Figure 5. a) Arrhenius plot for the catalysts; b) reaction rate of Pt/HMSs catalysts with different Pt particle sizes; c) typical shape of Pt NPs (insets show the fast Fourier transform pattern and diagram of the Pt shape); d) comparison of the experimental and calculated reaction rate based on different models.

size-insensitive. These results strongly imply that only one type of surface site dominates the reaction.[20]

To explore the dominant active site for the reaction, it was important to know how many types of sites were exposed on the Pt surface. By HRTEM, we found that the shape of a typical Pt nanoparticle is well represented by a truncated cuboctahedron (Figure 5c), which shows that there are four types of surface sites exposed on the surface of a Pt nanoparticle: corner sites, edge sites, (100) facets, and (111) facets. It is reasonable to assume that the activity of one type of specific site is independent of the Pt particle size. Thus, the total reaction rate will depend on the number of specific sites, which could be obtained by model calculations employing the truncated cuboctahedron shape.[21] The activity of one specific site is denoted as R_{site}, and the number of specific sites of this kind is denoted as N_{site} and N_{total}, respectively. The reaction rate, r_{CO}, can be calculated as follows:

$$r_{CO} = \frac{R_{site}N_{site}}{N_{total}} \tag{5}$$

The values of R_{site} for all types of surface site, that is, R_{corner}, R_{edge}, $R_{(100)}$, and $R_{(111)}$, were obtained by fitting the experimental results by a nonlinear regression method using the following equation:

$$RSS = \sum \left(r_{CO,\,exp} - r_{CO}\right)^2 \tag{6}$$

where $r_{CO,exp}$ represents the experimental data.

The fitted R_{site} value was used to calculate the reaction rate of differently sized Pt catalysts according to the specific site model. The calculated reaction rates based on different site models as a function of the Pt particle size are shown in Figure 5d with the experimental results. The reaction rate predicted by the corner model is proportional to d^{-3}, which is

very similar to the experimental results, that is, $d^{-3.6}$. The reaction rates calculated for edge, (100), and (111) models vary with the particle size as $d^{-1.4}$, $d^{0.23}$, and $d^{-0.4}$, respectively. These results suggest that, among of the surface sites, the corner sites dominate the reaction. DFT calculations were further carried out by using the Vienna Ab initio Simulation Package (VASP) to compare the activity of these four types of surface sites (see the Supporting Information for details). Figure 6 shows the energy profile for CO oxidation on these three model surfaces and a Pt_{13} cluster. The activation energy for CO oxidation on the Pt_{13} cluster is clearly lower than on the other surfaces, which agrees well with the experimental results that corner sites exhibit the highest activity for CO oxidation.
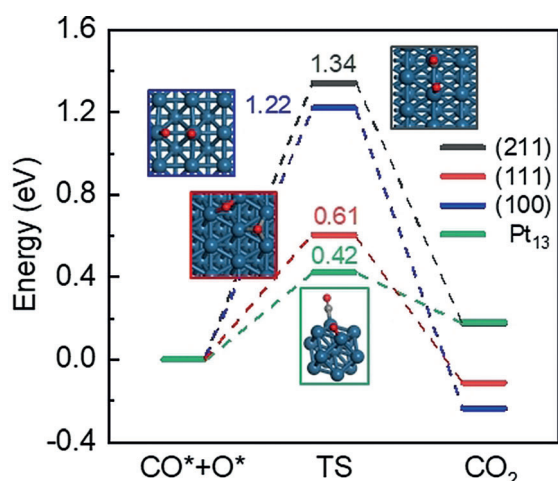

Figure 6. Potential energy diagram for CO oxidation on Pt(211), Pt-(111), Pt(100), and Pt_{13} cluster models (insets show the configurations of the transition states; see Figure S9 for the initial and final states).

Conclusion

A unique catalyst and sensor system (Pt/HMSs-BRC) was successfully fabricated by combining a Pt/HMSs catalyst with an adsorbed chromogenic probe (BRC). In this study, Pt/HMSs catalysts were synthesized by a facile vacuum-assisted incipient wetness impregnation method, and the results indicate that the Pt NPs were highly monodisperse and homogeneously dispersed, and mostly located in the pores of the HMSs. The CO oxidation activity of the catalysts was investigated as a function of Pt loading. The temperature for 100% CO conversion decreased as a function of increasing Pt loading. For 5 wt% Pt/HMSs, a temperature as low as 150°C was needed for 100% CO conversion. On the basis of these findings, the dominant active site for the reaction was explored by using a kinetics-assisted discrimination method and DFT calculations, which revealed that corner sites are the dominant active sites of Pt/HMSs for CO oxidation. At concentration thresholds at 50 ppm and above, when CO is considered toxic, a remarkable color change from gray-violet to light-yellow was observed after 70 s. The color of the system is fully recoverable in 60 min. Hence, the clear color change visible to the naked eye confirms the remarkable

sensing properties of the probe and suitable catalytic performance of the catalyst. This finding demonstrates the simultaneous detection and catalytic oxidation of CO. Adopting a combined catalyst and sensor system has the potential to be applied to detect and remove CO from air, and the reported dominant active sites for CO oxidation may have implications for the development of highly active catalysts.

Conflict of interest

The authors declare no conflict of interest.

[1] a) J. Lelieveld, J. S. Evans, M. Fnais, D. Giannadaki, A. Pozzer, *Nature* **2015**, *525*, 367; b) T. Salthammer, Y. Zhang, J. Mo, H. M. Koch, C. J. Weschler, *Angew. Chem. Int. Ed.* **2018**, *57*, 12228–12263; *Angew. Chem.* **2018**, *130*, 12406–12443.

[2] P. Q. Tan, Z. Y. Hu, M. di Lou, Z. J. Li, *Energy* **2012**, *39*, 356–362.

[3] a) S. Savagatrup, V. Schroeder, X. He, S. Lin, M. He, O. Yassine, K. N. Salama, X. X. Zhang, T. M. Swager, *Angew. Chem. Int. Ed.* **2017**, *56*, 14066–14070; *Angew. Chem.* **2017**, *129*, 14254–14258; b) C. Lin, X. Xian, X. Qin, D. Wang, F. Tsow, E. S. Forzani, N. Tao, *ACS Sens.* **2018**, *3*, 327–333.

[4] J. Esteban, J. V. Ros-Lis, R. Martínez-Máñez, M. D. Marcos, M. Moragues, J. Soto, F. Sancenón, *Angew. Chem. Int. Ed.* **2010**, *49*, 4934–4937; *Angew. Chem.* **2010**, *122*, 5054–5057.

[5] a) F. Li, H. C. Chan, S. Liu, H. Jia, H. Li, Y. Hu, Z. Wang, W. Huang, *Forensic Sci. Int.* **2015**, *253*, 112–118; b) X. Lu, F. Li, H. C. Chan, H. Jia, J. Dai, X. Ding, *Cogent Medicine* **2016**, *3*, 1137131; c) J. Ji, A. Kleinman, A. E. Becker, *Harvard Rev. Psychiatry* **2001**, *9*, 1.

[6] M. Strianese, C. Pellecchia, *Coord. Chem. Rev.* **2016**, *318*, 16–28.

[7] a) J. Zhang, L. Wang, B. Zhang, H. Zhao, U. Kolb, Y. Zhu, L. Liu, Y. Han, G. Wang, C. Wang, D. S. Su, B. C. Gates, F.-S. Xiao, *Nat. Catal.* **2018**, *1*, 540–546; b) X. P. Zou, L. N. Wang, X. N. Li, Q. Y. Liu, Y. X. Zhao, T. M. Ma, S. G. He, *Angew. Chem. Int. Ed.* **2018**, *57*, 10989–10993; *Angew. Chem.* **2018**, *130*, 11155–11159; c) L. N. Wang, X. N. Li, L. X. Jiang, B. Yang, Q. Y. Liu, H. G. Xu, W. J. Zheng, S. G. He, *Angew. Chem. Int. Ed.* **2018**, *57*, 3349–3353; *Angew. Chem.* **2018**, *130*, 3407–3411.

[8] a) A. Garg, M. Milina, M. Ball, D. Zanchet, S. T. Hunt, J. A. Dumesic, Y. Román-Leshkov, *Angew. Chem. Int. Ed.* **2017**, *56*, 8828–8833; *Angew. Chem.* **2017**, *129*, 8954–8959; b) I. X. Green, W. Tang, M. Neurock, J. T. Yates, Jr., *Science* **2011**, *333*, 736–739.

[9] Z. Zhang, Y. Zhu, H. Asakura, B. Zhang, J. Zhang, M. Zhou, Y. Han, T. Tanaka, A. Wang, T. Zhang, *Nat. Commun.* **2017**, *8*, 16100.

[10] a) M. J. Hazlett, M. Moses-Debusk, J. E. P. Ii, L. F. Allard, W. S. Epling, *Appl. Catal. B* **2017**, *202*, 404–417; b) A. M. Gänzler, M. Casapu, P. Vernoux, S. Loridant, A. Fjcs, T. Epicier, B. Betz, R. Hoyer, J. D. Grunwaldt, *Angew. Chem. Int. Ed.* **2017**, *56*, 13078–13082; *Angew. Chem.* **2017**, *129*, 13258–13262; c) R. Rizo, D. Sebastián, M. J. Lázaro, E. Pastor, *Appl. Catal. B* **2017**, *200*, 246–254.

[11] a) L. Nie, D. Mei, H. Xiong, B. Peng, Z. Ren, H. Xip, A. Delariva, M. Wang, M. H. Engelhard, L. Kovarik, *Science* **2017**, *358*, 1419–1423; b) C. Yang, Z. Wang, X. Zhou, X. Tian, Z. Pi, Y. Wang, *J. Porous Mater.* **2011**, *18*, 31–35; c) S. Krick Calderón, M. Grabau, J. E. Yoo, M. Killian, P. Schmuki, H. P. Steinrück, C. Papp, *ChemCatChem* **2017**, *9*, 564–572; d) X. Wei, B. Shao, Y. Zhou, Y. Li, C. Jin, J. Liu, W. Shen, *Angew. Chem. Int. Ed.* **2018**, *57*, 11289–11293; *Angew. Chem.* **2018**, *130*, 11459–11463; e) Y. Wang, H. Gao, *J. Phys. Chem. B* **2017**, *121*, 2132–2141.

[12] a) P. A. Zhizhko, A. V. Pichugov, N. S. Bushkov, F. Allouche, A. A. Zhizhin, D. N. Zarubin, N. A. Ustynyuk, *Angew. Chem. Int. Ed.* **2018**, *57*, 10879–10882; *Angew. Chem.* **2018**, *130*, 11045–11048; b) A. Wong, Q. Liu, S. Griffin, A. Nicholls, J. R. Regalbuto, *Science* **2017**, *358*, 1427–1430.

[13] J. Després, M. Elsener, M. Koebel, O. Kröcher, B. Schnyder, A. Wokaun, *Appl. Catal. B* **2004**, *50*, 73–82.

[14] Y. Hu, Y. Wang, Z. H. Lu, X. Chen, L. Xiong, *Appl. Surf. Sci.* **2015**, *341*, 185–189.

[15] a) R. Eckert, M. Felderhoff, F. Schüth, *Angew. Chem. Int. Ed.* **2017**, *56*, 2445–2448; *Angew. Chem.* **2017**, *129*, 2485–2488; b) Y. Suchorski, S. M. Kozlov, I. Bespalov, M. Datler, D. Vogel, Z. Budinska, K. M. Neyman, G. Rupprechter, *Nat. Mater.* **2018**, *17*, 519–522; c) S. Gupta Chatterjee, S. Chatterjee, A. K. Ray, A. K. Chakraborty, *Sens. Actuators B* **2015**, *221*, 1170–1181; d) S. Vetter, S. Haffer, T. Wagner, M. Tiemann, *Sens. Actuators B* **2015**, *206*, 133–138.

[16] Y. Chen, H. Chen, L. Guo, Q. He, F. Chen, J. Zhou, J. Feng, J. Shi, *ACS Nano* **2010**, *4*, 529–539.

[17] W. Ding, H. Zhuo, M. Bao, Y. Li, J. Lu, *Chem. Eng. J.* **2017**, *330*, 337–344.

[18] A. R. Chakravarty, F. A. Cotton, D. A. Tocher, J. H. Tocher, *Organometallics* **1985**, *4*, 8–13.

[19] X. Feng, X. Duan, G. Qian, X. Zhou, D. Chen, W. Yuan, *J. Catal.* **2014**, *317*, 99–104.

[20] a) W. Chen, J. Ji, X. Feng, X. Duan, G. Qian, P. Li, X. Zhou, D. Chen, W. Yuan, *J. Am. Chem. Soc.* **2014**, *136*, 16736–16739; b) W. Fu, W. Chen, G. Qian, D. Chen, W. Yuan, X. Zhou, X. Duan, *React. Chem. Eng.* **2019**, *4*, 316–322; c) Y. Cao, W. Fu, Z. Sui, X. Duan, D. Chen, X. Zhou, *Ind. Eng. Chem. Res.* **2019**, *58*, 1888–1895.

[21] R. Van Hardeveld, F. Hartog, *Surf. Sci.* **1969**, *15*, 189–230.
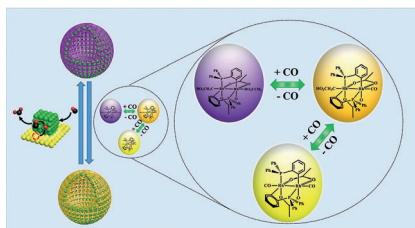
Research Articles

Carbon Monoxide Sensors

J. Qu, Y. Cao, X. Duan, N. Li, Q. Xu, H. Li,
J. He, D. Chen,* J. Lu* ──── ▪▪▪▪–▪▪▪▪

Eye-Readable Detection and Oxidation of
CO with a Platinum-Based Catalyst and
a Binuclear Rhodium Complex

Now you see it, now you don't: A chromogenic probe was adsorbed onto silica gel and combined with a Pt catalyst supported on hollow mesoporous silica spheres (HMSs) for the simultaneous detection and catalytic conversion of CO (see picture). The Pt/HMSs catalyst was able to convert 100% of the CO, and the chromogenic probe displayed a remarkable color change at CO concentration levels above 50 ppm.